ELSEVIER

Electroencephalography and clinical Neurophysiology 107 (1998) 93–111

Improving source reconstructions by combining bioelectric and biomagnetic data

Manfred Fuchs[a,*], Michael Wagner[a], Hans-Aloys Wischmann[a], Thomas Köhler[a], Annette Theißen[a], Ralf Drenckhahn[a], Helmut Buchner[b]

[a]*Philips Research Laboratories Hamburg, Röntgenstrasse 24, D-22335 Hamburg, Germany*
[b]*Department of Neurology, RWTH, Pauwelsstrasse 30, D-52074 Aachen, Germany*

Accepted for publication: 2 March 1998

Abstract

Objectives: A framework for combining bioelectric and biomagnetic data is presented. The data are transformed to signal-to-noise ratios and reconstruction algorithms utilizing a new regularization approach are introduced.

Methods: Extensive simulations are carried out for 19 different EEG and MEG montages with radial and tangential test dipoles at different eccentricities and noise levels. The methods are verified by real SEP/SEF measurements. A common realistic volume conductor is used and the less well known in vivo conductivies are matched by calibration to the magnetic data. Single equivalent dipole fits as well as spatio-temporal source models are presented for single and combined modality evaluations and overlaid to anatomic MR images.

Results: Normalized sensitivity and dipole resolution profiles of the different EEG/MEG acquisition systems are derived from the simulated data. The methods and simulations are verified by simultaneously measured somatosensory data.

Conclusions: Superior spatial resolution of the combined data studies is revealed, which is due to the complementary nature of both modalities and the increased number of sensors. A better understanding of the underlying neuronal processes can be achieved, since an improved differentiation between quasi-tangential and quasi-radial sources is possible. © 1998 Elsevier Science Ireland Ltd. All rights reserved

Keywords: Electroencephalogram; Magnetoencephalogram; SEP; SEF; Source reconstruction; Regularization; Boundary element method

1. Introduction

Source reconstructions combining bioelectric and biomagnetic data promise to benefit from the advantages of both modalities (Cohen and Cuffin, 1979, 1983, 1987, 1991; Cohen et al., 1990; Lopes da Silva et al., 1991; Mauguiere, 1992). Electroencephalographic (EEG) measurements can be carried out with an optimized electrode arrangement and provide nearly equal sensitivities for tangentially- and radially-oriented sources. Due to this unspecific sensitivity distribution EEG data often suffer from a limited signal-to-noise-ratio (SNR) and exhibit rather complex field structures. Magnetoencephalographic (MEG) gradiometer systems have an increased sensitivity for tangential superficial sources, leading to an improved SNR and a larger specificity for this class of generators. On the other hand this means that MEG sensor arrays are more or less blind to (quasi-)radial neural current components and deep sources, leading to a reduced complexity of the measured field patterns. Therefore, a combination of both complementary methods should be able to reveal radial dipole components and stabilize the reconstruction of tangential sources by an increased information content and an improved overall SNR.

In order to combine both modalities in a unified framework, different problems have to be solved:

- The different measures have to be transformed to a common basis. This is done by referencing each sensor to its individual noise statistics (Greenblatt, 1995; Pflieger et al., 1998). So every measurement channel contributes with its statistical relevance to the ensuing evaluation procedures. One method to

* Corresponding author. Tel.: +49 40 50782691; fax: +49 40 50782887.

0013-4694/98/$19.00 © 1998 Elsevier Science Ireland Ltd. All rights reserved
PII S0013-4694(98)00046-7

automatically determine the noise level of each sensor is to use the standard deviation of a fraction of the smallest signal levels of the total latency range, e.g. the smallest 20%. This method of course requires about 20% signal-free (e.g. pre-trigger) samples in the measurement.

- For unified reconstruction algorithms, a common volume conductor model has to be used. EEG data strongly depend on the head's shape and its conductivities (Cuffin, 1990). For example, in volume conductor models with one compartment only, the measured signals are inversely proportional to the conductivity. MEG signals in the spherical volume conductor approximation are not at all affected by the conductivity. With more realistically-shaped volume conductor models (e.g. boundary element method (BEM) models) the MEG data show only a weak dependence on the electric properties of the compartments. Furthermore the individual real (in-vivo) tissue conductivities are not well known (Geddes and Baker, 1963). We have thus chosen latencies where single dominantly tangential dipoles can explain the measured data very well for both modalities and used them for matching the conductivities of the volume conductor model. Thus the magnetic data are used for calibrating the electric conductivities via a common scaling factor that keeps the relative conductivities of the model compartments (brain, skull, skin) constant.
- MEG reconstructions with realistic volume conductor models tend to overemphasize quasi-radial current components due to their very small gain (Menninghaus and Lütkenhöner, 1995). Therefore, dipole regularization techniques have to be introduced in order to limit or suppress these low-gain components at least in single-modality MEG evaluations. In EEG or combined EEG/MEG examinations, the electric data are expected to reduce these effects due to their nearly isotropic orientational sensitivity distributions (Fuchs et al., 1998b).

For testing the methods described above in view of their spatial resolution, simulations with different electrode and magnetometer/gradiometer set-ups were used with a 3 spherical shells volume conductor model. White noise, uncorrelated across sensors, was added to calculated field distributions to get statistically relevant results for different dipole depths and signal-to-noise-ratios. Equivalent dipolar sources were then fitted with single and combined modalities.

Evoked somatosensory measurements from electric medianus nerve stimulation with simultaneously recorded 31 electrodes EEG (SEP) and 31 channels MEG (SEF) (Buchner et al., 1994) were used to test combined evaluations with real data. The volume conductor was modeled by a BEM consisting of 3 compartments. The head/brain compartments for the BEM model were semi-automatically segmented, and triangulated from magnetic resonance (MR) images (Wagner et al., 1995). Single equivalent dipoles, cortically constrained deviation scans (Fuchs et al., 1994, 1998a), and spatiotemporal dipole models (Scherg and von Cramon, 1985; Mosher et al., 1992) were used to compare single modality and merged evaluations.

2. Methods

2.1. Signal-to-noise-ratio transformation

In order to combine the different measures of electric and magnetic data, both have to be converted to a common basis. Using their signal-to-noise-ratios (SNRs) (Greenblatt, 1995; Pflieger et al., 1998) all sensor or sensor group signals are processed in the ensuing reconstruction algorithms according to their statistical significances. A channel-wise SNR transformation can be utilized by determination of the noise amplitude n_i of eac[illegible] (e.g. pre-trigger) latency ranges. From these periods with t_n timepoints (samples) the noise amplitudes can be estimated from the standard deviations of the measured signals $m_{ij} = m_i(t_j)$:

$$n_i = \sqrt{\frac{1}{t_n - 1}\sum_{t_n}\left(m_{ij} - \overline{m}_i\right)^2} \quad \text{with} \quad \overline{m}_i = \sum_{t_n} m_{ij} \Big/ t_n \tag{1}$$

Constant channel offsets are compensated by subtraction of the mean-values $\overline{m}_i$. Linear drifts of the signals can be compensated by subtracting linear best-fit functions, which are calculated per channel from continuous signal-free periods:

$$n_i = \sqrt{\frac{1}{t_n - 2}\sum_{t_n}\left(m_{ij} - \left(a_i t_j + b_i\right)\right)^2}$$

$$\text{with} \quad a_i = \frac{\sum_{t_n} m_{ij} t_j - t_n \overline{m}_i \overline{t}}{\sum_{t_n} t_j^2 - t_n \overline{t}^2},\ b_i = \overline{m}_i - a_i \overline{t},\ \overline{t} = \sum_{t_n} t_j \Big/ t_n \tag{2}$$

The timepoints used for the noise estimation can also be taken from histographic analyses of the data (e.g. *x*% percentile). Another possibility, assuming 'white' noise spectra, is to use the signal-free high-frequency part of the data and extrapolate the spectral noise power for all frequencies of the given measurement bandwidth. In multi-epoch data the noise characteristics could also be estimated by more sophisticated techniques, e.g. by taking single trial statistics into account.

Finally the signal-to-noise-ratios are calculated by normalization of the measured signals to their individual noise amplitudes, yielding unit-free measures for both electric and magnetic modalities, that can be combined for merged reconstructions:

$$\hat{m}_{ij} = m_{ij} \Big/ n_i \tag{3}$$

In cases, where the channel-wise noise determination is not well-suited, due to a low number of signal-free samples, a group-wise noise normalization is possible. Here a common mean noise level $\bar{n}_g$ is used for all sensors of one modality (s_e, number of electrodes; s_m, number of magnetometers):

$$\bar{n}_e = \sum_{s_e} n_{ie} / s_e \text{ and } \bar{n}_m = \sum_{s_m} n_{im} / s_m \quad (4)$$

The forward calculation of the electromagnetic fields has, of course, to be modified accordingly (see below).

2.2. Forward models

To solve the inverse problem, that is reconstructing the generators of the measured data, appropriate models have to be used. The neural sources are modeled by equivalent or elementary dipoles, for which analytical or numerical expressions exist, that describe their electromagnetic field distributions. These formulas depend on the position and orientation of the dipolar source, the position (and orientation, in the magnetic case) of the sensors, and the volume conductor model and its conductivities. For example in infinite homogeneous volume conductors (conductivity σ_0, permeability μ_0) there are very simple analytic expressions for the electric potential V_0 and the magnetic field $\underline{B}_0$ (dipole at position $\underline{r}_j$, current $\underline{j}$, sensor at position $\underline{r}$):

$$V_0 = \frac{1}{4\pi\sigma_0}\,\underline{j}\,\frac{\underline{r}-\underline{r}_j}{|\underline{r}-\underline{r}_j|^3} \quad (5)$$

$$\underline{B}_0 = \frac{\mu_0}{4\pi}\,\underline{j}\times\frac{\underline{r}-\underline{r}_j}{|\underline{r}-\underline{r}_j|^3} \quad (6)$$

In the magnetic case, normally only one field component is measured by the sensor coils. The coil normal direction $\underline{e}_s$ (weighted by the coil area a_s) has to be multiplied to the magnetic field resulting in the calculated magnetic signal B:

$$B = a_s\underline{e}_s\underline{B}_0 = a_s\underline{e}_s\left(\frac{\mu_0}{4\pi}\,\underline{j}\times\frac{\underline{r}-\underline{r}_j}{|\underline{r}-\underline{r}_j|^3}\right) \quad (7)$$

In both electric and magnetic cases, the fields depend linearly on the current, $\underline{j}$. This holds also for the more complicated spherical shell formulas (de Munck, 1988) or more realistic volume conductor models.

The boundary element method (BEM) allows calculation of the electric potential, V and the magnetic field, $\underline{B}$ of a current source in an inhomogeneous conductor by the following two integral equations, if the conducting object is divided by closed surfaces $S_i (i = 1,...,n_s)$ into n_s compartments, each having a different enclosed isotropic conductivity σ_i^{in}. The electric potential at position $\underline{r} \in S_k$ is then given by the following formula (Geselowitz, 1967, 1970; Sarvas, 1987):

$$\bar{\sigma}_k V(\underline{r}) = \sigma_0 V_0(\underline{r}) + \frac{1}{4\pi}\sum_{i=1}^{n_s}\Delta\sigma_i \oint\!\!\oint_{S_i} V(\underline{r}')\underline{n}(\underline{r}')\cdot\frac{\underline{r}'-\underline{r}}{|\underline{r}'-\underline{r}|^3}dS_i' \quad (8)$$

Given the solution of Eq. (8), the resulting magnetic field for $\underline{r} \notin S_k$ is:

$$\underline{B}(\underline{r}) = \underline{B}_0(\underline{r}) + \frac{\mu_0}{4\pi}\sum_{i=1}^{n_s}\Delta\sigma_i \oint\!\!\oint_{S_i} V(\underline{r}')\underline{n}(\underline{r}')\times\frac{\underline{r}'-\underline{r}}{|\underline{r}'-\underline{r}|^3}dS_i' \quad (9)$$

with V_0 and B_0 representing the potential and the magnetic field of the source in an unlimited homogeneous medium with conductivity σ_0 (see above), the mean conductivity $\bar{\sigma}_k = \left(\sigma_k^{in} + \sigma_k^{out}\right)/2$ and the conductivity differences $\Delta\sigma_i = \sigma_i^{in} - \sigma_i^{out}$. To calculate the electromagnetic fields it is necessary to numerically approximate the two integrals over the closed surfaces S_i of the conductor boundaries consisting of differential surface elements (dS_i') and with surface normal orientations, $\underline{n}$, at positions $\underline{r}'$. The surfaces are described by a large number of small triangles and the integrals are replaced by summations over these triangle areas. Different assumptions about the variation of the potential over the triangle area can be applied (van Oosterom and Strackee, 1983; de Munck, 1992; Ferguson et al., 1994; Schlitt et al., 1995): averaged, regionally constant, linear, and quadratic dependencies. The potential values or the coefficients of the basis functions, used to approximate the potentials on the surface elements, form a vector of unknowns which can be solved through the following matrix formulations:

$$\underline{\underline{\bar{\sigma}}}\,\underline{V} = \sigma_0\underline{V}_0 + \underline{\underline{A}}\,\underline{V} \Rightarrow \underline{V} = (\underline{\underline{\bar{\sigma}}} - \underline{\underline{A}})^{-1}\sigma_0\underline{V}_0 \quad (10)$$

$$\underline{\underline{B}} = \underline{\underline{B}}_0 + \underline{\underline{C}}\,\underline{V} \Rightarrow \underline{\underline{B}} = \underline{\underline{B}}_0 + \underline{\underline{C}}\left(\underline{\underline{\bar{\sigma}}} - \underline{\underline{A}}\right)^{-1}\sigma_0\underline{V}_0 \quad (11)$$

If one explicitly solves Eqs. (10) and (11) just for the fixed number of measurement positions, a transfer matrix is obtained, that relates the sensor signals to the homogeneous potentials/fields (e.g. Fletcher et al., 1995).

2.3. Lead-field formulation

Due to the linearity in the dipole components of all volume conductor models, the so called lead-field formulation provides a more compact notation comprising all $s = s_e + s_m$ sensor signals in column vectors:

$$\underline{V} = \underline{\underline{L}}_V\underline{j} \text{ and } \underline{B} = \underline{\underline{L}}_B\underline{j} \quad (12)$$

The lead-field matrices $\underline{\underline{L}}_V(3*s_e)$ and $\underline{\underline{L}}_B(3*s_m)$ contain all geometric information, such as dipole and sensor positions, and volume conductor properties, whereas the linear dipole components $\underline{j}$ and thereby the dipole orientations are separated.

To combine both modalities, a common lead-field matrix has to be set up after the transformation to common units (signal-to-noise-ratios) has been performed. For that purpose, each calculated sensor signal is normalized by its individual noise amplitude determined from the measured data as described above (n_{ie} and n_{im}, Eqs. (1)–(4)). Then the columns of magnetic lead-field matrix (s_m sensors (rows)) are appended to the corresponding columns of the electric

lead-field matrix (s_e sensors (rows)). The measured data, $\underline{M}$, are treated similarly:

$$\underline{\underline{L}}\,\underline{j} = \begin{bmatrix} \underline{\underline{\hat{L}}}_{\mathrm{V}} \\ \underline{\underline{\hat{L}}}_{\mathrm{B}} \end{bmatrix} \underline{j} = \begin{bmatrix} \hat{l}_{\mathrm{V1x}} & \hat{l}_{\mathrm{V1y}} & \hat{l}_{\mathrm{V1z}} \\ \cdots & \cdots & \cdots \\ \hat{l}_{\mathrm{Vs_e x}} & \hat{l}_{\mathrm{Vs_e y}} & \hat{l}_{\mathrm{Vs_e z}} \\ \hat{l}_{\mathrm{B1x}} & \hat{l}_{\mathrm{B1y}} & \hat{l}_{\mathrm{B1z}} \\ \cdots & \cdots & \cdots \\ \hat{l}_{\mathrm{Bs_m x}} & \hat{l}_{\mathrm{Bs_m y}} & \hat{l}_{\mathrm{Bs_m z}} \end{bmatrix} \begin{bmatrix} j_{\mathrm{x}} \\ j_{\mathrm{y}} \\ j_{\mathrm{z}} \end{bmatrix}$$

$$\text{and } \underline{\underline{M}} = \begin{bmatrix} \underline{\underline{\hat{M}}}_{\mathrm{V}} \\ \underline{\underline{\hat{M}}}_{\mathrm{B}} \end{bmatrix} = \begin{bmatrix} \hat{m}_{\mathrm{1e}} \\ \cdots \\ \hat{m}_{\mathrm{s_e e}} \\ \hat{m}_{\mathrm{1m}} \\ \cdots \\ \hat{m}_{\mathrm{s_m m}} \end{bmatrix} \tag{13}$$

In a spatiotemporal formulation, the vector, $\underline{M}$, containing the measured data, has to be extended to a matrix $\underline{\underline{M}}$, where each column vector represents one sample. Accordingly the current component vector, $\underline{j}$, has to be extended. For keeping the expressions better readable, the vector and matrix underlines are omitted in the following equations ($\underline{j} \rightarrow j$, $\underline{\underline{L}} \rightarrow L$, $\underline{\underline{M}} \rightarrow M$).

2.4. Conductivity matching

The combination of electric and magnetic data for merged reconstructions with real measured data may fail, since the exact in-vivo values of the electric conductivities are not well known (Geddes and Baker, 1963). The calculated electric fields are inversely proportional to the conductivity of the source space for simple volume conductor geometries (infinite homogeneous conductors or spheres) and depend on the conductivity ratios and differences for more complicated and more realistic models (spherical shells and BEM). The magnetic fields of simple models (infinite homogeneous media, or spherically symmetric conductors) do not at all depend on the electric conductivities and for more realistic models there is only a weak dependency on the conductivity ratios of the BEM model compartments used.

To overcome this problem, the absolute conductivity values can be scaled by a common factor, so that the conductivity ratios remain unchanged and the electric potentials are affected by this approach only. This factor can then be fitted as an additional non-linear parameter during the minimization procedure that optimizes the dipole position(s) (see below). In order to obtain a reliable result for the conductivity matching factor, latencies or latency ranges should be used, where good signal-to-noise-ratios of both data modalities have been acquired, a single tangentially oriented dipolar source is dominant, and where a low residual fit variance can be achieved. The conductivities are not assumed to depend on the source orientations and the timepoint, so their fitted values will be used throughout the entire evaluation procedure and for any reconstruction algorithms.

2.5. The inverse problem

The best-fit solution of the inverse problem is determined by minimizing the residual variance Δ^2 (squared deviation) between the measured data and the forward calculated fields using the Frobenius norm of an (m*n) matrix A:

$$|A|^2 = \sum_{i=1}^{m} \sum_{k=1}^{n} a_{\mathrm{ik}}^2 \tag{14}$$

$$\Delta^2 = |M - Lj|^2 \tag{15}$$

M is the spatiotemporal measured data matrix (s sensors*t samples), the lead-field matrix L (s*c current dipole components) comprises the dipole positions, the volume conductor characteristics, and the sensor geometry, and j contains the (c*t) temporal loadings or strengths of the ($c = 3$*d dipoles) dipole components. The best-fit currents, $\hat{j}$, that minimize Eq. (15) in the overdetermined case (more knowns than unknowns: $s > c$) are given by (Lawson and Hanson, 1974; Ben-Isreal and Greville, 1976):

$$\hat{j} = \left(L^{\mathrm{T}} L\right)^{-1} L^{\mathrm{T}} M \tag{16}$$

The best-fit dipole positions can be found by non-linear minimization algorithms (e.g. Nelder–Mead simplex (Nelder and Mead, 1965)). For each dipole position or configuration the lead-field matrix, L, has to be set up and the best-fit deviation (Eq. (15) with $j = \hat{j}$) is calculated by solving the linear problem for the dipole strengths (Eq. (16)). The minimizer changes the non-linear parameters (the dipole positions) and looks for the global minimum of the error hypersurface.

2.6. Generalized error function

A generalized formulation for the minimum norm solution of the inverse problem can be written as follows:

$$\Delta^2 = |D(M - Lj)|^2 + \lambda^2 |Cj|^2 \tag{17}$$

Here the variance Δ^2 consists of the weighted (by λ^2) sum of the data term $|D(M - Lj)|^2$ and the minimum norm model term $|Cj|^2$. M, L, and j are defined as above (Eq. (15)). A weighting of the sensors can be applied by the (s*s) matrix D, whereas a weighting of the current dipole components is described by the (c*c) matrix, C. The best-fit solution, $\hat{j}$, that minimizes Eq. (17) in the overdetermined case is given by (Lawson and Hanson, 1974):

$$\hat{j} = C^{-1}\left(C^{-1T}L^{T}D^{T}DLC^{-1} + \lambda^{2}\right)^{-1}C^{-1T}L^{T}D^{T}DM \qquad (18)$$

2.7. Singular value decomposition of the lead-field matrix

Analyzing the unweighted lead-field matrix, L, by performing a singular value decomposition (SVD) (Press et al., 1992) yields the principal dipole components, their gains, and their partial field-patterns. In the magnetic case for one dipole and a boundary element method (BEM) model of the human head the quasi-tangential and the low-gain quasi-radial dipole orientations can thus be determined (Fuchs et al., 1998b). Small gain dipole components have to be regularized to avoid overemphasizing of the corresponding current strengths.

The solution of the linear problem (matrix inversion in Eqs. (16) and (18)) can be found by performing an SVD of the (weighted) lead-field matrix, $\tilde{L} = DLC^{-1}$, and the regularization can be applied:

$$\tilde{L} = U\Sigma V^{T} \text{ with } U^{T}U = 1 \text{ and } V^{T}V = VV^{T} = 1 \qquad (19)$$

The orthonormal matrix, $U(s*c)$, contains the principal normalized field-patterns, the diagonal matrix, $\Sigma(c*c)$, the corresponding gains (gain of the ith component: $\sigma_i = \sigma_{ii}$), and the orthonormal rotation matrix, $V^{T}(c*c)$ the principal dipole orientations.

The generalized minimum norm solution is found by inserting Eq. (19) into Eq. (18):

$$\hat{j} = C^{-1}V\Sigma^{-1}\Omega U^{T}DM \qquad (20)$$

with the diagonal regularization matrix

$$\Omega = \left[\frac{1}{1 + \lambda^{2}/\sigma_i^{2}}\right] \qquad (21)$$

The bracketed term symbolizes a diagonal matrix (ith element) derived from the ith element of the diagonal gain matrix (σ_i) and the regularization parameter, λ.

The term $U^{T}DM(c*t)$ comprises the projections of the weighted, normalized principal field patterns (generated by the principal dipole components) onto the weighted, measured data. Regularization takes place in the unique principal coordinate system (rotated by V^{T}). The (real-world) dipole current components are recovered by back-rotation into the original coordinate system (by matrix V in Eq. (20)).

The best-fit variance in the generalized form follows by insertion of Eq. (20) into Eq. (17):

$$\Delta^{2} = \sum_{k=1}^{t} M_k^{T}D^{T}DM_k - \sum_{k=1}^{t} M_k^{T}D^{T}U\Omega U^{T}DM_k \qquad (22)$$

with the kth column of the spatiotemporal data matrix M denoted as M_k (so the summations are over all t samples). This formula shows that the minimum residual variance, Δ^2, is the difference between the total data variance (squared, weighted measured data, DM) and the forward calculated, explainable variance, consisting of the squared, regularized (by Ω) projections ($U^{T}DM$) of the field patterns (U^{T}), that are generated by the principal dipole components, onto the weighted data, DM.

2.8. Standard minimum norm weights

From now on we will consider two special cases of the current components weighting without any sensor weighting ($D = 1$). First the standard minimum norm case ($C = 1$) will be discussed. In this case the unweighted lead-field matrix is decomposed ($\tilde{L} = L = U\Sigma V^{T}$), and the best-fit solution of Eq. (17) is:

$$\hat{j} = V\Sigma^{-1}\Omega U^{T}M \qquad (23)$$

leading to

$$\Delta^{2} = \sum_{k=1}^{t} M_k^{T}M_k - \sum_{k=1}^{t} M_k^{T}U\Omega U^{T}M_k \qquad (24)$$

The remaining problem in this case is to find the correct value of the regularization parameter λ. One possibility is to determine λ by the so called L-curve method, i.e. by plotting data- against model-term on double logarithmic scales as a function of λ and choosing λ from the point of largest curvature (Hansen, 1992). The units of λ are gain factors $(\text{nAm})^{-1}$, principal dipole components with gains of $\sigma_i = \lambda$ will be damped by a factor of $\omega_i = 0.5$ (Eq. (21), Fig. 1).

Special care has to be taken for the tendency of minimum norm solutions to overemphasize sources close to the sensors (Crowley et al., 1989; Gorodnitzky et al., 1992), because they can generate similar fields at lower loadings compared to more distant sources. This leads to an increased data-term, but a decreased model-term in Eq. (17), so that the sum of both becomes minimal at more superficial source locations. In order to compensate for this effect at least partially, an appropriate lead-field normalization should be introduced (Lawson and Hanson, 1974; Köhler et al., 1996).

2.9. A new measure for minimum norm weighting

A second method of current component weighting is to use the projections of their field patterns (U^{T}) onto the measured data and in that way their ability to explain these data and minimize the rest variance Δ^2 (Eqs. (22) and (24)). This is done by choosing the model term matrix according to:

$$C = WV^{T} \text{ and } C^{-1} = VW^{-1} \qquad (25)$$

with the diagonal weighting matrix, W, that weights the principal current dipole components (which are determined by an SVD of the weighted lead-field matrix $DL = U\Sigma V^{T}$) according to their projections ($U^{T}DM$) and their gains σ_i:

$$w_i = \sigma_i \Big/ \sqrt{\sum_{k=1}^{t} M_k^{T}D^{T}U_iU_i^{T}DM_k} \qquad (26)$$

The ith diagonal element of W (w_i) is calculated from the

projections of U_i (the ith column of U, containing the field pattern generated by the ith principal dipole component ($V^T j_i$)) onto the weighted, measured data DM. The denominator of Eq. (26) represents the partial contribution of the ith principal dipole component to the explainable total deviation. From Eq. (18) it follows for this special case:

$$\hat{j} = V\Sigma^{-1}\tilde{\Omega}U^T DM \tag{27}$$

with the diagonal matrix

$$\tilde{\Omega} = \left[\frac{1}{1+\lambda^2 w_i^2/\sigma_i^2}\right] = \left[\left(1+\lambda^2 \Big/ \sum_{k=1}^{t} M_k^T D^T U_i U_i^T D M_k\right)^{-1}\right] \tag{28}$$

and a residual variance expression similar to Eq. (24) with Ω replaced by this regularization matrix. With this new method, the regularization parameter is now in the units of the measured data (SNRs). Principal dipole components that explain a partial variance of λ^2 (or a partial deviation of λ) will be damped by a factor of $\omega_i = 0.5$ (Eq. (28), Fig. 1). If the noise in the data is estimated correctly, a value of $\lambda = 1$ should be a good choice, since then those components are damped, that can produce statistically-insignificant contributions to the measured data only. Thus a long-lasting search for the correct value of the regularization parameter is avoided and a more practical measure is used instead of the abstract dipole gains of the standard method.

Furthermore, lead-field normalization is less critical compared to the standard minimum norm scheme, since the new, more indirect measure punishes insignificant contributions without using the component's gains, instead of suppressing low-gain components leading to large strengths in the model terms. The applicability of this new regularization technique to underdetermined problems (minimum norm least squares/current density reconstructions) will be the subject of another publication (work in progress).

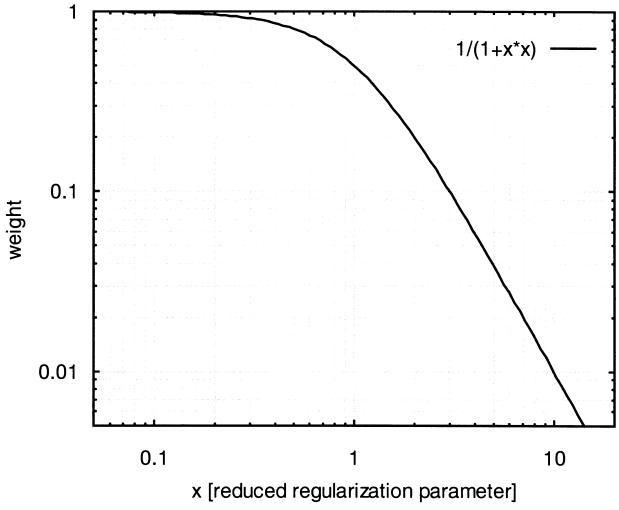

Fig. 1. Regularization weights ω_i (compare Eqs. (21) and (28)) as a function of the reduced regularization parameter $x = \lambda/\sigma_i$. For small reduced parameters no damping occurs, for $x = 1$ the weight is 0.5, and for large parameter values strong attenuation takes place ($\approx x^{-2}$).

2.10. .Simulations

Simulations with tangentially- and radially-oriented test dipoles were carried out for 19 different EEG and MEG sensor configurations representing high-to-low number electrode montages as well as a full coverage whole head magnetometer system to a low coverage first-order gradiometer system (Fig. 2). Three spherical shells fitted to the electrodes have been used as volume conductor model (radii: 85, 92, 100 mm; conductivities: 0.33, 0.0042, 0.33 $(\Omega m)^{-1}$). Forward calculations were performed for radial and tangential test dipoles at 12 different heights (depths in vertical direction) ranging from –30 to 80 mm (center of the volume conductor at 0 mm, stepsize 10 mm). White noise was added to the calculated field distributions and averaging was performed in order to get statistically-relevant results for mean SNRs and mean dipole mislocalizations. From each test position, 200 field-patterns have been derived by adding noise of a fixed variance. In order to simulate different quality measurements, 5 noise classes were generated by selecting different noise amplitudes. At the largest eccentricity (94%) the noise was adjusted to yield mean SNRs of about 100, 50, 20, 10, and 5 for the different sensor configurations. Overall 460 000 field patterns were calculated and the same number of dipole fits was performed.

The different sensor set-ups could thus be tested for their depth sensitivities and their equivalent dipole localization accuracy in single as well as in combined modality evaluations. Due to the spherical test volume conductor symmetry in the magnetic case tangential dipoles could be used only. For the mixed EEG + MEG studies also tangential dipoles were used only, since the magnetic data would yield no additional information for radial sources (SNR = 0).

2.11. .Evoked somatosensory field examinations

In order to verify the simulation results with real measured data, a standard SEP/SEF experiment was used. The left medianus nerve of a female, right-handed subject was electrically stimulated at the wrist with an intensity of twice the motor threshold. Rectangular current pulses of 0.2 ms duration and a repetition frequency of 3.1 Hz were used (Buchner et al., 1994). The electric (31 electrodes) and magnetic (31 first-order gradiometers (PHILIPS MEG)) signals were sampled over periods of 128 ms pre- and 128 ms post-stimulus with a sampling rate of 1k Hz. The data were filtered in a frequency range from 5 to 200 Hz. Four replications of 1000 epochs each were averaged for SNR improvement.

The electrodes were unevenly distributed across the head to improve spatial sampling over the right somatosensory

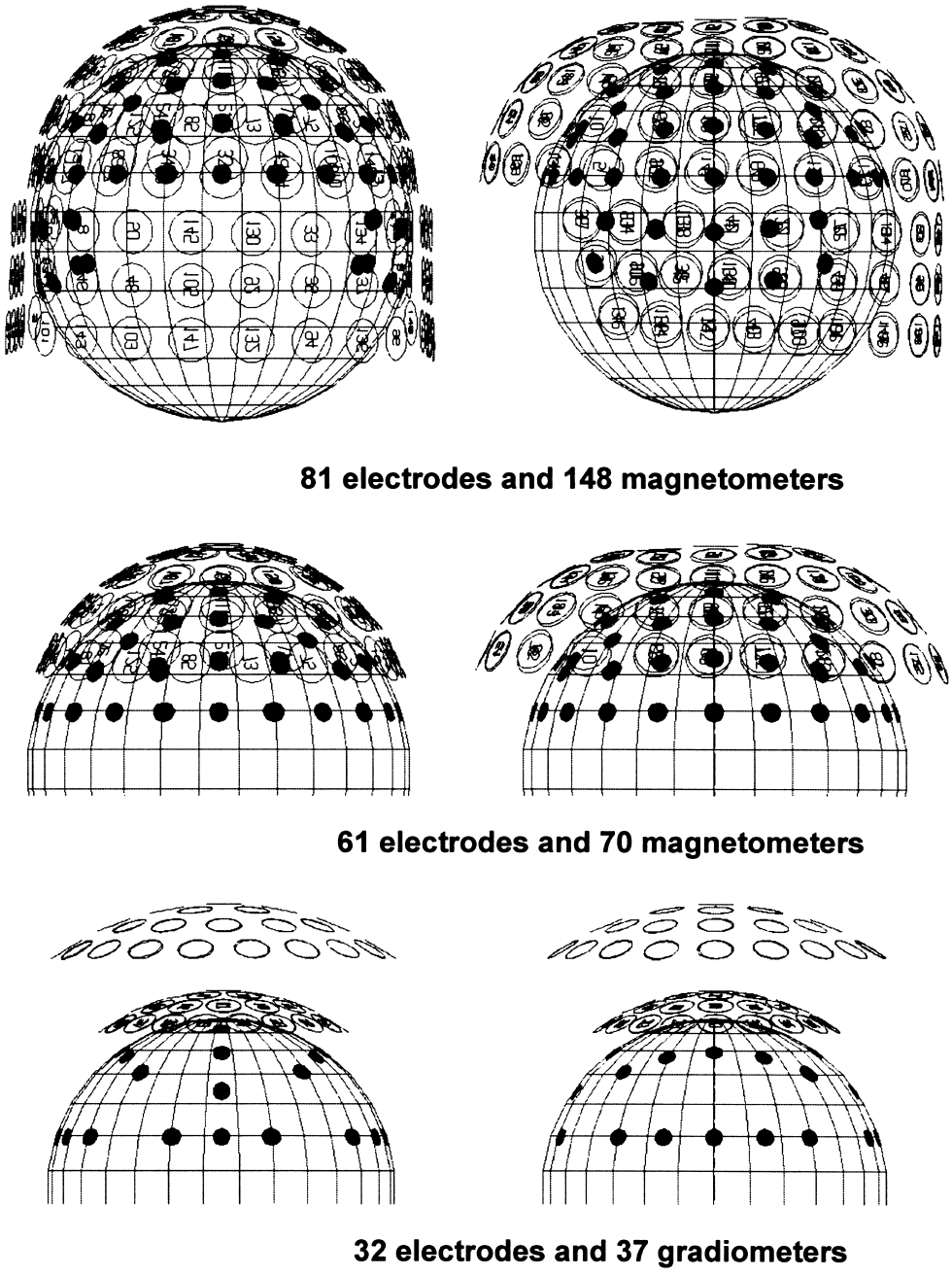

Fig. 2. Sensor set-ups used for the EEG and MEG simulations with 3 spherical shells volume conductor models. Left column: frontal views, right column: left side views.

areas corresponding to left medianus nerve stimulation (Figs. 3 and 10). The reference electrode was placed at Fz, the measured data were finally rereferenced to a common average reference and the same procedure was applied to the calculated potentials.

The electrode positions as well as 4 additional landmarks for registration of the MEG cryostat were marked with fat capsules that produce a good contrast in magnetic resonance (MR) images. The landmarks were replaced by magnetic coilsets, that were localized before and after each session by the MEG system (Fuchs et al., 1995). For the anatomical data-set 128 sagittal MR slices (1.6 mm thick) with an image matrix of 256×256 pixels and a field of view of 300 mm were taken with a 1.5 T system and a strongly T_1-weighted gradient echo pulse sequence.

2.11.1. BEM model setup

The evoked somatosensory measurements were analyzed with both modalities combined, and compared to the corresponding single modality evaluations. In all cases a realistically-shaped volume conductor model (BEM) was used. The MR data were interpolated to an isotropic data cube and the skin surface with the electrode markers was segmented by radial raycasting from the outside (Fig. 3). The electrode

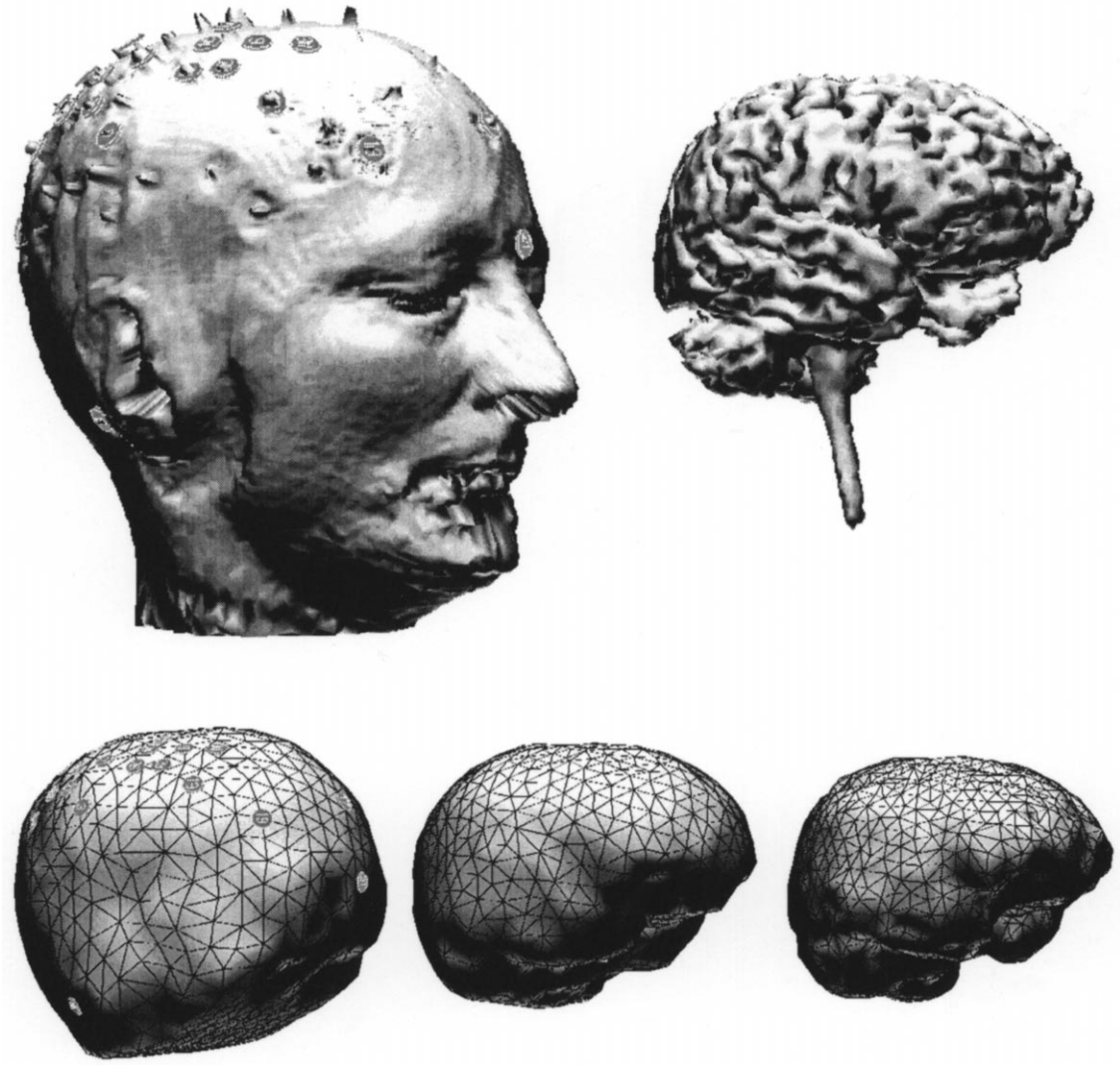

Fig. 3. Head and brain surfaces segmented from 3D MR data. Upper row: skin with electrodes and cortical gray matter layer. Lower row: 3 BEM compartments: skin (12 mm mean triangle edge length, 755 nodes), outside skull (10 mm, 805 nodes), and inside skull (8 mm, 1212 nodes).

positions were read out by a mouse-controlled cursor in a 5-side-views presentation of this surface. The cortical surface was segmented by 3D region growing with a single intensity threshold value representing the border layer between white and gray matter. The 3 BEM model compartments were also segmented from the MR data starting with the inside of the skull, which was approximated by a smoothed, dilated envelope of the gray matter layer. The outside of the skull was then found by filling the first compartment with pass-markers (which are transparent for region growing), a dilation of about 7 mm and converting the outside to stop-markers (which block the region growing) to avoid bleeding to the lower parts of the head, followed finally by region growing with a threshold value representing the border between bone and skin and a smoothing operation. The skin itself was segmented by filling the skull-compartment with pass-markers, further dilation of 14 mm, setting the outside to stop-markers, region growing with a threshold of the skin–air transition, and smoothing.

To get a triangular representation of the compartment surfaces needed for the BEM-meshes and visualization purposes, the surfaces were thinned with different radii (8 mm for the liquor/brain-, 10 mm for the skull-, and 12 mm for the skin-compartment, Fig. 3). This procedure yielded a total of 2772 nodes (5532 triangles) for the BEM-model with 1212 nodes (2420 triangles) for the innermost compartment, that was treated separately, in an isolated problem approach (IPA) (Hämäläinen and Sarvas, 1989). The set-up time for both IPA-BEM matrices ($2772^2 \Rightarrow 61.4$ MB and $1212^2 \Rightarrow 11.8$ MB storage requirement) with a linear potential approximation (Schlitt et al., 1995) over virtually refined triangles (Fuchs et al., 1998b) took about 9 min on an UltraSparc 1/170 workstation with 128 MB memory. The LU-decomposition of the BEM matrices and the set-up of the transfer matrices containing all sensor positions (and orientations for the MEG) needed about 2 min altogether.

2.11.2. Source reconstruction methods

Single moving dipole reconstructions representing the centers of the (in this case overlapping) cortical activations of the tangentially oriented N20 and the radially oriented P22 generators were overlaid onto the MR data of the subject and the segmented cortical surface. In addition, cortically-constrained deviation scans (Fuchs et al., 1998a) were performed at different latencies for the single and merged modality cases and spatiotemporal methods (Scherg and von Cramon, 1985; Mosher et al., 1992) were applied. The deviation scans were carried out on the segmented gray matter layer surface with mean support point distances of 2.3 mm for a patch containing the upper part of the right hemisphere only (3135 points). At each node of this cortical surface representation the best-fit residual deviation (Eq. (22)) was calculated and 1-deviation was plotted in a color-coded fashion (Fig. 9), so 1 corresponds to 0% relative deviation (perfect fit) and 0 to 100% deviation (no fit possible). The cortically constrained MUSIC scan was performed on all 18 681 nodes of the whole brain surface (mean node distance 3.3 mm). The surface normals, which could have been used to further constrain the reconstructions in view of the dipole orientations, were not taken into account.

The single equivalent dipole fits as well as the cortically constrained deviation scans were performed at latencies between 18 and 24 ms, so the onset of the tangentially-oriented N20 and the transition to the radially oriented P22 was covered. The spatiotemporal approaches were applied for the whole interesting latency range of 10–60 ms and up to 3 fixed dipole sources have been calculated sequentially. In this approach, the dominating tangential dipole patterns in the latency range of 18–21 ms were fitted first by a fixed dipole. Next, the mixed tangential/radial patterns in the time-range from 22 to 26 ms were fitted with a second fixed dipole, while keeping the first, already-fitted dipole, fixed in position and orientation. Finally, a third dipole was fitted in the range from 14 to 17 ms, keeping both previously-fitted dipoles fixed in position and orientation. Then, with all 3 sources fixed, their strengths and residual variances were determined for all samples from 10 to 60 ms. The results of this approach depend on the order of the time-ranges chosen and their extents, and were thus compared to the more objective MUSIC scan results. The source volume for all dipole fits was restricted to the inside of the innermost boundary element compartment (inside of the skull).

3. Results

3.1. Simulations

First the mean SNRs were plotted against the depths of the dipoles. Thus the depth sensitivities of the different single and combined modality set-ups can be studied by analyzing the reduced SNRs, which are equivalent to the relative system sensitivities. The mean SNR values of the most superficial dipole position were used for normalization. After performing single dipole fits, the mean mislocalizations (averaged spatial distances between true and fitted dipole positions) were plotted as a function of the test dipole depths. Fig. 4 displays the sensitivity results for all single modality set-ups. On the semi-logarithmic scaling nearly linear dependencies can be found for the EEG montages, visualizing an exponential decrease of the SNRs with dipole depth.

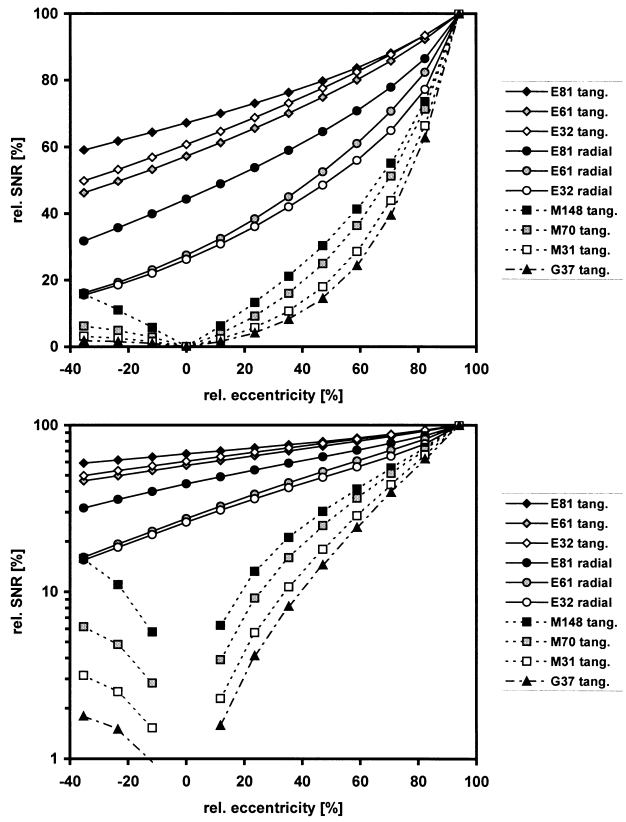

Fig. 4. Normalized SNRs (system sensitivities) for different EEG montages (E81, E61, and E32) with tangentially and radially oriented test dipoles in a 3 spherical shells volume conductor model. The MEG simulations for different magnetometer/gradiometer set-ups (M148, M70, M31, and G37) were performed with tangential test dipoles only. The upper part shows a linear SNR scale, while the lower part has a logarithmic scale to better visualize the small SNR values.

The EEG simulations with 3 different montages (81, 61 and 32 electrodes, Fig. 2) were analyzed for radially- and tangentially-oriented test dipoles. As expected, the slopes differ for different montages and different dipole orientations. For the largest coverage set-up with 81 electrodes, the SNRs of dipoles at the center position drop to 44%, 62% and 72% compared to the most superficial position for radial, front–back tangential, and left–right tangential source orientations. The results for front–back oriented tangential dipoles are very similar to the results for the left–right oriented tangential sources, thus their averages are displayed only. With smaller coverage (61 and 32 electrode

montages), the mean sensor sensitivities drop slightly faster (to 27% for the radial and to about 58% for the tangential dipole orientations). No significant dependency on the electrode density (spatial sampling) could be found when comparing the 61 and 32 sensor set-ups. The differences between the 81 electrodes montage and the lower sensor number set-ups, especially for radial dipoles, has its reason in the smaller coverage of those systems, so that the signals of deeper radial sources cannot be detected as well as by the full coverage system.

The results for the different MEG systems are shown for tangential source orientations only. The shielding effects of the volume conductor can clearly be seen in the sharply decreasing SNRs with depth (approaching 0 at the center of the sphere). This decrease is over-exponential for deep sources, which are consequently suppressed and cannot be localized very well. The 1st order gradiometer system exhibits the steepest SNR versus depth slope and is therefore worst for localizing deeper dipoles.

The combined EEG + MEG results are displayed in Fig. 5. Again, tangentially oriented dipoles were used only. The SNRs at small eccentricities are dominated by the electric signals, whereas at larger eccentricities, both modalities contribute. The number of sensors of one modality makes up its weight in the averaging. This is the reason why the 81 electrodes combined with 70 or 31 magnetometers have a slower decrease in sensitivity than the combination with 148 magnetic sensors. For the latter the faster-decreasing MEG sensitivity dominates, whereas for the other configurations the 81 electrodes 'win'.

The corresponding mean dipole mislocalizations are displayed in Figs. 6 and 7. Of course their order is reversed compared to the mean SNRs, meaning that the best SNR test positions have the smallest localization error and that these errors increase for decreasing SNRs and thus decreasing eccentricities. The localization errors were found to be inversely proportional to the mean SNRs for all 5 measurement quality classes (SNRs <100, <50, <20, <10 and <5). Therefore the curves in Figs. 6 and 7 were normalized to the mean SNRs. This allows to universally use these plots for the estimation of confidence intervals for fitted single dipoles, given the sensor montage, the dipole depth, and the data-SNR (if no systematic errors are present).

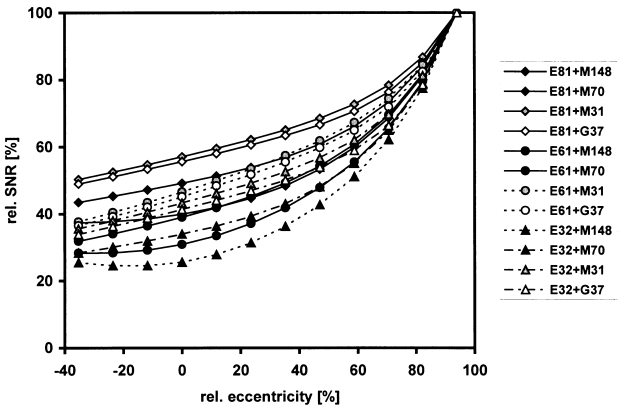

Fig. 5. Normalized SNRs (system sensitivities) for combined EEG + MEG simulations with tangentially oriented dipoles. All combinations of the 3 different electrode montages (E81, E61, and E32) with the 4 different magnetometer/gradiometer systems (M148, M70, M31, and G37) are displayed.

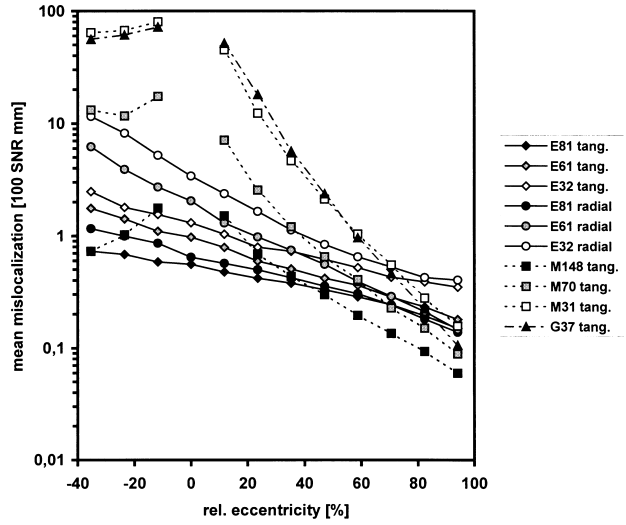

Fig. 6. Normalized dipole mislocalizations for different EEG and MEG set-ups (compare Figs. 2 and 4) as a function of the test dipole depth. For a given SNR all curves have to be scaled by a factor of 100/SNR to get the mean fit errors in mm. The MEG simulations (M148, M70, M31, and G37) were performed with tangentially oriented dipoles only.

For sources at larger eccentricities the increased resolution of the MEG systems can be seen, compared to the electric cases (the corresponding curves cross each other). Taking into account that EEG data often suffer from lower SNRs (by a factor of about two, see SEP/SEF example), the crossover-points will slightly shift towards smaller eccentricities for real world applications.

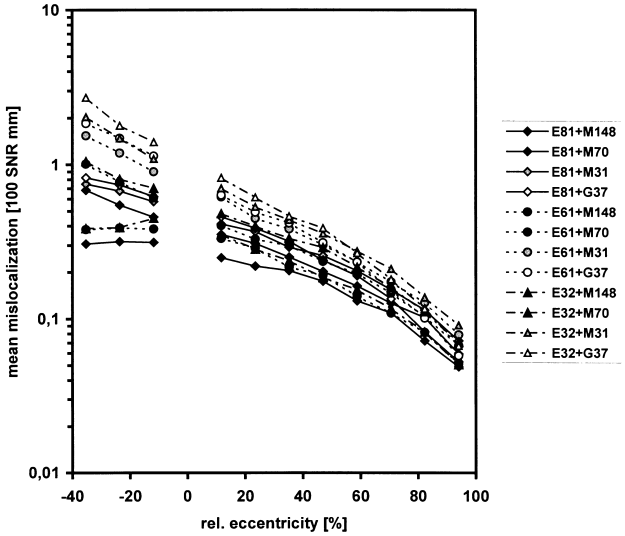

Fig. 7. Normalized dipole mislocalizations for different combined EEG + MEG set-ups (compare Figs. 2 and 5) as a function of the test dipole depth. For a given SNR all curves have to be scaled by a factor of 100/SNR to get the mean fit errors in mm. All simulations were performed with tangentially oriented dipoles only.

In the MEG case a more prominent saturation of the mislocalizations for deep sources can be found, compared to the EEG case. This is due to the restriction of the sources to the inside of the spherical volume conductor. These artifacts have been omitted in Fig. 6, but the effect can be estimated easily by comparing the sphere radius to the large mislocalizations of the MEG systems at low eccentricities.

The results of the combined EEG + MEG evaluations can be seen in Fig. 7. Due to the larger number of sensors and the complementary field distributions, the combined results are always better than the corresponding single modality evaluations. For superficial source positions the superior magnetic localization power (compared to the EEG cases)

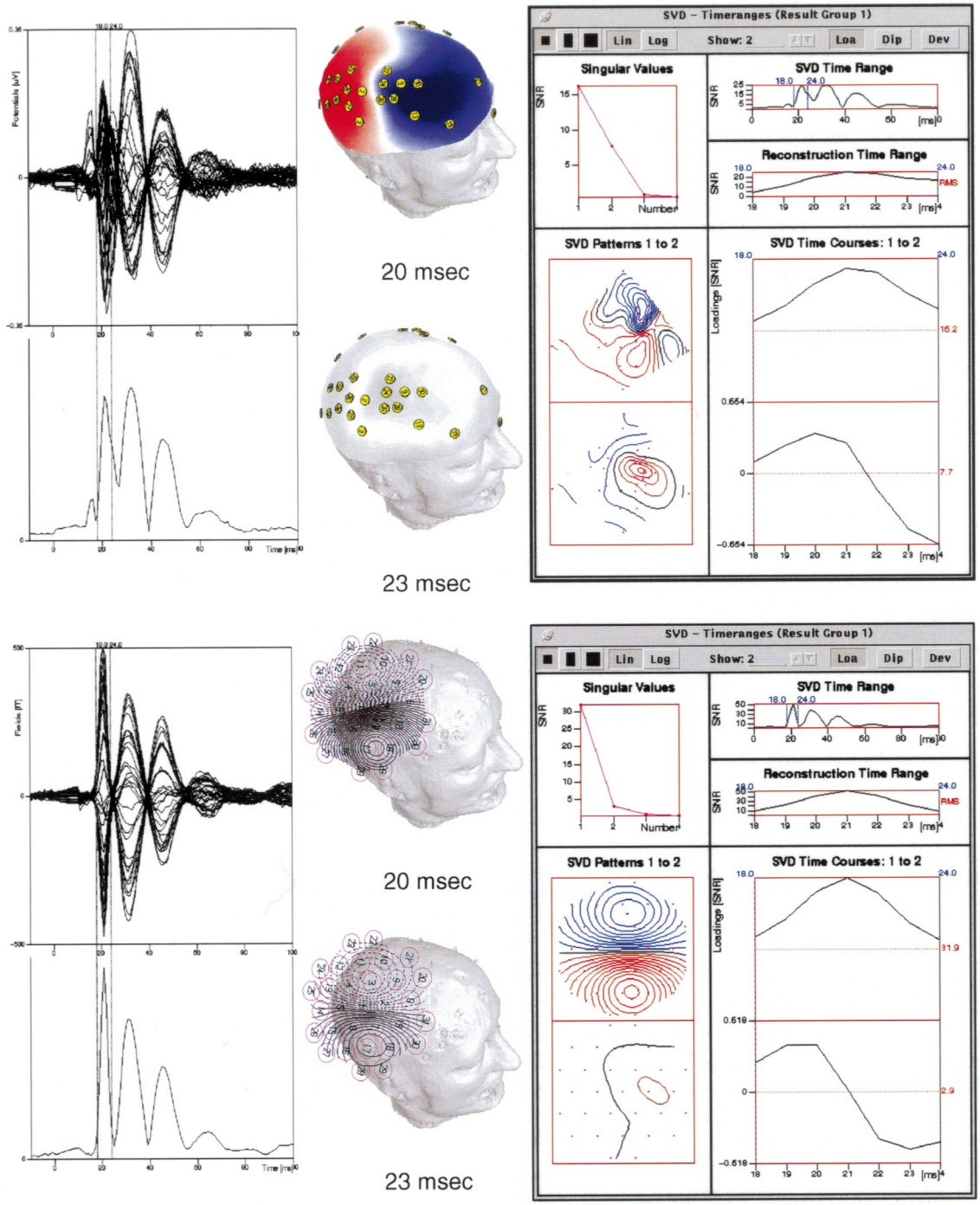

Fig. 8. Butterfly-plots (from –10 to 100 ms) of the measured signals evoked by electric medianus nerve stimulation, mean global field powers, and potential/field-maps (middle column). The right column displays SVD analyses of the selected time range (18–24 ms) with contour maps (left) and time courses (right) of the two dominant field patterns. Upper half: 31 electrodes EEG (somatosensory evoked potentials (SEP)), lower half: 31 gradiometers MEG (somatosensory evoked fields (SEF)).

is further improved by the additional information content of the electric channels. The steep increase in localization errors of the MEG systems alone for deeper sources cannot be found in the merged studies, where the electric data are capable of localizing deep sources with smaller errors.

3.2. Evoked somatosensory field examinations

The measured EEG data are displayed in Fig. 8, together with field-maps at two selected latencies (20 and 23 ms) and singular value decomposition (SVD) analyses of the time range, that was selected for source reconstructions (18–24 ms). For comparison, the corresponding MEG data are analyzed and displayed in the same fashion in the lower part of Fig. 8. The noise amplitudes were estimated in the pre-trigger periods of both data (from −120 to −10 ms). The EEG data are noisier (max. SNR: 25) than the MEG data (max. SNR: 52) and exhibit several structures that cannot be found in the MEG traces. For example, the small peak at latencies around 15 ms and the shoulder

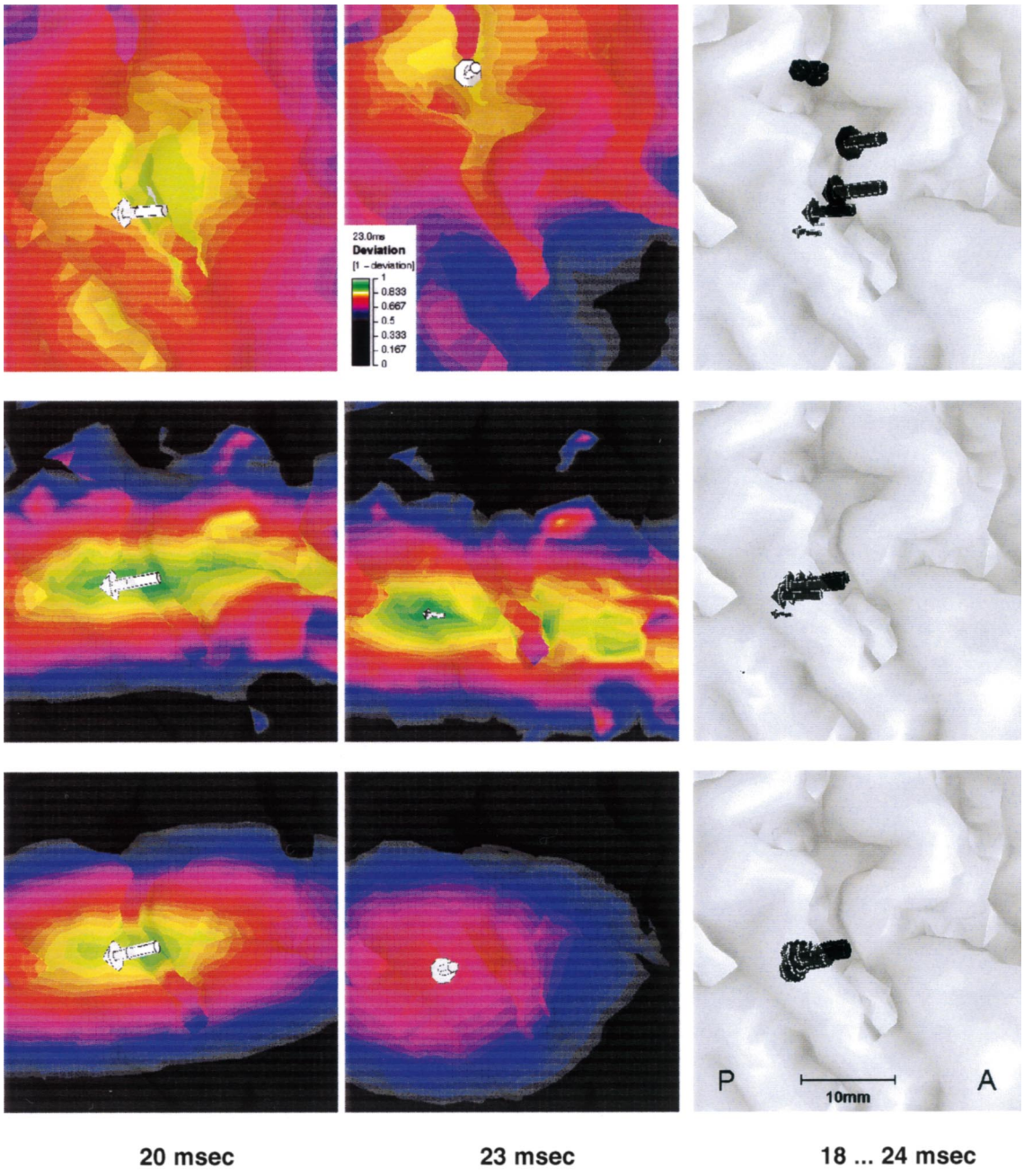

Fig. 9. Single moving dipole reconstructions (at 20, 23, and 18–24 ms) with an enlarged view of the right central sulcus (upper left to lower right). First row: EEG data only, middle row: MEG data only, lower row: EEG + MEG used together. Left and middle columns: two single latency dipole reconstructions together with cortically constrained, color-coded deviation scans, right column: dipoles for all latencies overlaid with a rendering of the cortical gray matter layer.

at the decreasing slope of the first large peak around 24 ms are missing in the MEG signals. Furthermore, the different amplitude ratios of the large peaks are obvious. All these features can be explained by the missing sensitivity of the MEG sensors to (quasi-) radially oriented source components.

3.2.1. Single equivalent dipoles and cortically constrained deviation scans

The SVD analyses show, that in the selected latency range two EEG patterns (one apparently tangential, and one apparently radial) are present, which are comparable in amplitude (around 2:1), whereas in the MEG case one pattern is clearly dominating (amplitude ratio 10:1).

Before the dipole reconstructions and deviation scans were performed, a factor for matching the conductivities of the BEM volume conductor model was fitted at latencies around 20 ms, where a tangential source clearly dominates both EEG and MEG data. Fig. 9 shows single moving dipole reconstructions at two selected latencies (20 and 23 ms), when tangential and radial patterns are pre-dominant in the EEG data, and for the whole selected latency range (18–24 ms). For visualization of the anatomical correlation an enlarged view of the cortical surface segmented from the MR data is overlaid. The right central sulcus can clearly be identified (anterior: right, posterior: left, compare Fig. 3 field-maps).

In order to verify the dipole fit results and to show confidence regions (provided that there are no systematic errors like sensor mislocalizations, oversimplified volume conductor models or incorrect source models) for the single dipole solutions, cortically constrained deviation scans are also displayed as color-coded surfaces together with the single latency dipoles.

At all latencies the single dipole source model was able to explain the measured data very well in both EEG and MEG cases (best fit at 21 ms: EEG: 11.8% relative deviation (normalized to the measured data) = 1.4% residual variance, MEG: 4.9% dev. = 0.2% res. var., EEG + MEG: 7.7% dev. = 0.6% res. var.). Details can be found in Table 1, where source locations for single and combined modality evaluations are compared to the results of EEG + MEG with regularization. At a latency of 20 ms all modalities without and with regularization yield the same result for the tangential source (largest distance 0.6 mm). The dipole

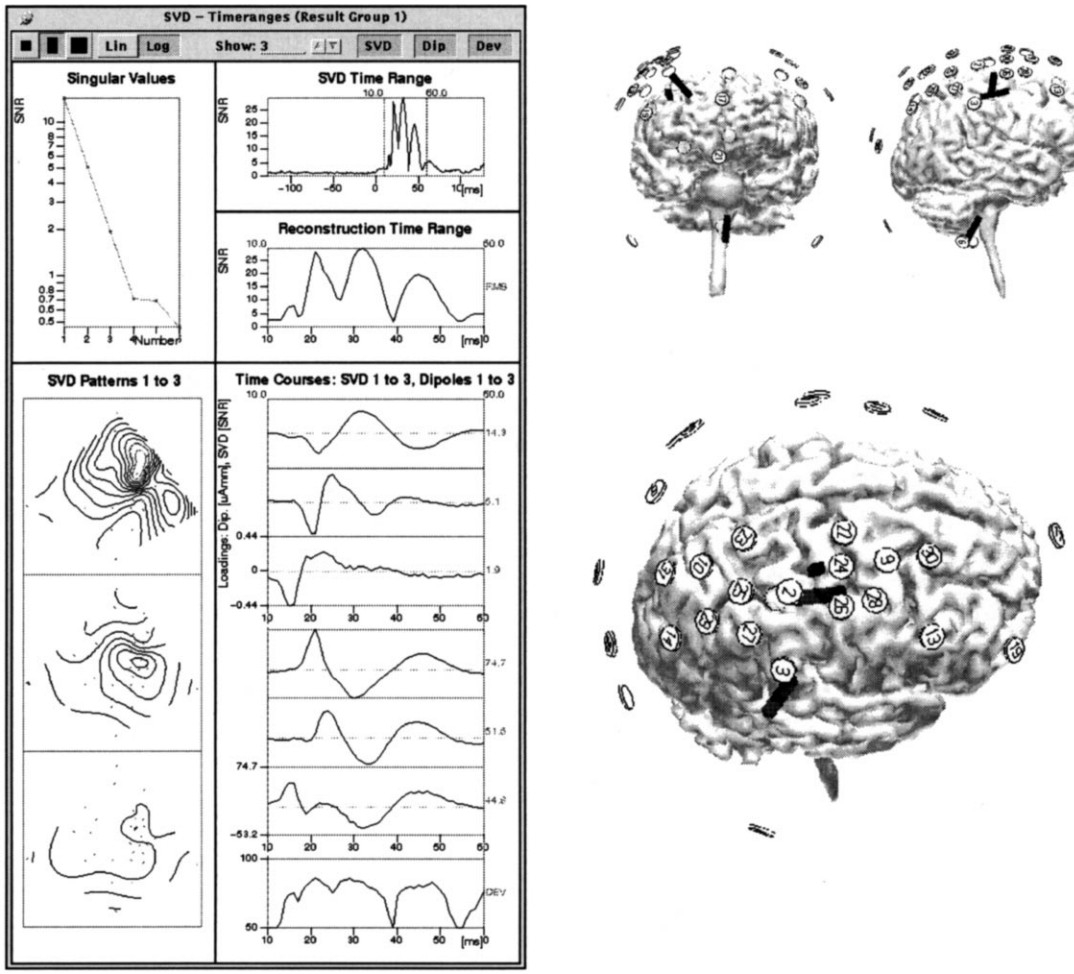

Fig. 10. Spatiotemporal analysis of the EEG data in the latency range of 10–60 ms. On the left side, the leading 3 SVD field-patterns and -loadings can be seen together with the loadings of 3 sequentially-fitted fixed dipoles and the explained deviation (lowest row). The right column displays the dipole positions and orientations (shown as dark bars) overlaid to the cortical surface and the electrodes in different projections.

Table 1
Results of single moving dipole fits in the latency range of 18–24 ms for EEG (SEP), MEG (SEF), and both, without (regul. 0) and with regularization

Latency (ms)	EEG regul. 0			Regul. 1		MEG regul. 0			Regul. 1.5		EEG + MEG regul. 0			Regul. 1
	SNR	Dev (%)	Dr (mm)	Dev (%)	Dr (mm)	SNR	Dev (%)	Dr (mm)	Dev (%)	Dr (mm)	SNR	Dev (%)	Dr (mm)	Dev (%)
18	4.4	19.2	5.9	23.8	9.6	9.3	8.8	2.0	10.5	2.1	7.3	14.8	1.3	15.8
19	10.9	21.0	3.1	21.1	2.1	22.5	7.5	0.4	8.1	2.4	17.7	13.3	0.6	13.6
20	20.0	13.0	0.6	13.2	0.3	41.9	6.2	0.6	6.2	0.5	32.8	8.6	0.1	8.6
21	25.0	11.7	4.2	11.8	4.2	52.3	4.7	1.4	4.9	1.6	41.0	7.7	0.0	7.7
22	23.2	14.1	8.4	14.2	8.5	41.1	4.8	3.3	5.0	3.5	33.3	10.9	0.0	10.9
23	17.9	14.2	13.9	14.3	14.2	19.7	7.8	6.7	7.9	6.2	18.9	20.4	0.5	20.5
24	15.8	15.9	13.1	15.9	13.1	7.6	20.6	14.8	21.3	14.2	12.4	32.0	0.2	32.0

The SNRs, residual deviations (Dev), and spatial deviations (Dr) of the dipole locations from the reference result (EEG + MEG with regularization) are displayed.

positions differ for the single modality results (compare Fig. 9), especially at latencies with lower SNRs (e.g. MEG at 24 ms). These results have larger confidence regions and are thus not well defined. Furthermore at the later timepoints the radial dipole develops in the EEG data, and therefore the EEG dipole positions differ as well from the MEG and the combined results.

Regularization affects mainly the latencies with lower SNRs at the beginning and the end of the analyzed peak by suppressing insignificant contributions to the residual variance. Thus the explained variances are slightly smaller with regularization (compare also Table 2) and the dipole positions are shifted.

The EEG dipoles exhibit a transition from a tangential source at 20 ms located in the posterior wall of the central sulcus to a radial source at a latency of 23 ms. The confidence regions of the reconstructions are larger and more isotropic as compared to the MEG case. There the typical ellipsoidal shape with a narrow confidence range perpendicular to the dipole direction and smaller specificity along its direction (and in the depth, which cannot be clearly seen in Fig. 9) can be found. The MEG dipoles are all tangentially oriented and are rather stable in position (except for latencies with very small SNRs).

The combined evaluations (Fig. 9, lowest row) profit from both EEG and MEG properties. At latencies where the tangential component is dominating, an improved spatial resolution compared to both single modality evaluations can be seen with a confidence area shape similar to the MEG case (since the SNR of the MEG data is twice as large as in the EEG data, the MEG data dominate at this latency). At later latencies, when the radial dipole comes up in the EEG data and when in the MEG case only the decreasing tangential dipole component can be reconstructed, the EEG data dominate and determine the dipole orientation and the more isotropic confidence region. The remaining MEG signals of the decreasing tangential source force the radial dipole position towards lower locations, thus deteriorating the common fit quality due to an inadequate source model (two different sources are present with overlapping activation profiles).

Table 2
Results of the spatiotemporal dipole fits for all modalities without (regul. 0) and with regularization

Latency (ms)	MEG			EEG				EEG + MEG			
	Max SNR			EEG regul. 0 (best res. dev. 11.7%)				EEG regul. 1 (best res. dev. 13.3%)			
				dx	*dy*	*dz*	*dr*	*dx*	*dy*	*dz*	*dr*
14–17	5.6	3.2	4.2	–21.8	–19.7	–11.1	31.4	–20.4	–39.9	–9.9	45.9
18–21	25.0	52.3	41.0	–1.7	1.5	0.1	2.3	1.2	–1.4	0.3	1.9
22–26	23.2	41.1	33.3	–4.2	–0.5	8.9	9.9	–2.3	–2.4	8.4	9.0

Latency (ms)	MEG regul. 0 (best res. dev. 6.4%)				MEG regul. 1 (best res. dev. 6.7%)				EEG + MEG regul. 0 (best res. dev. 8.2%)			
	dx	*dy*	*dz*	*dr*	*dx*	*dy*	*dz*	*dr*	*dx*	*dy*	*dz*	*dr*
14–17									–12.6	–11.7	8.7	19.3
18–21	–0.7	– 0.6	0.5	1.0	–0.8	–0.3	0.7	1.1	0.0	–0.1	0.0	0.1
22–26									0.1	0.2	–1.4	1.4

Three dipoles were successively fitted in the latency ranges of 18–21 ms, 22–26 ms, and 14–17 ms (in this order). The spatial deviations of the sources from the reference result (EEG (SEP) + MEG (SEF) with regularization) are given in mm. In the MEG cases only one tangential dipole was fitted. The *x*-axis points from right to left, the *y*-axis from anterior to posterior and the *z*-axis upwards.

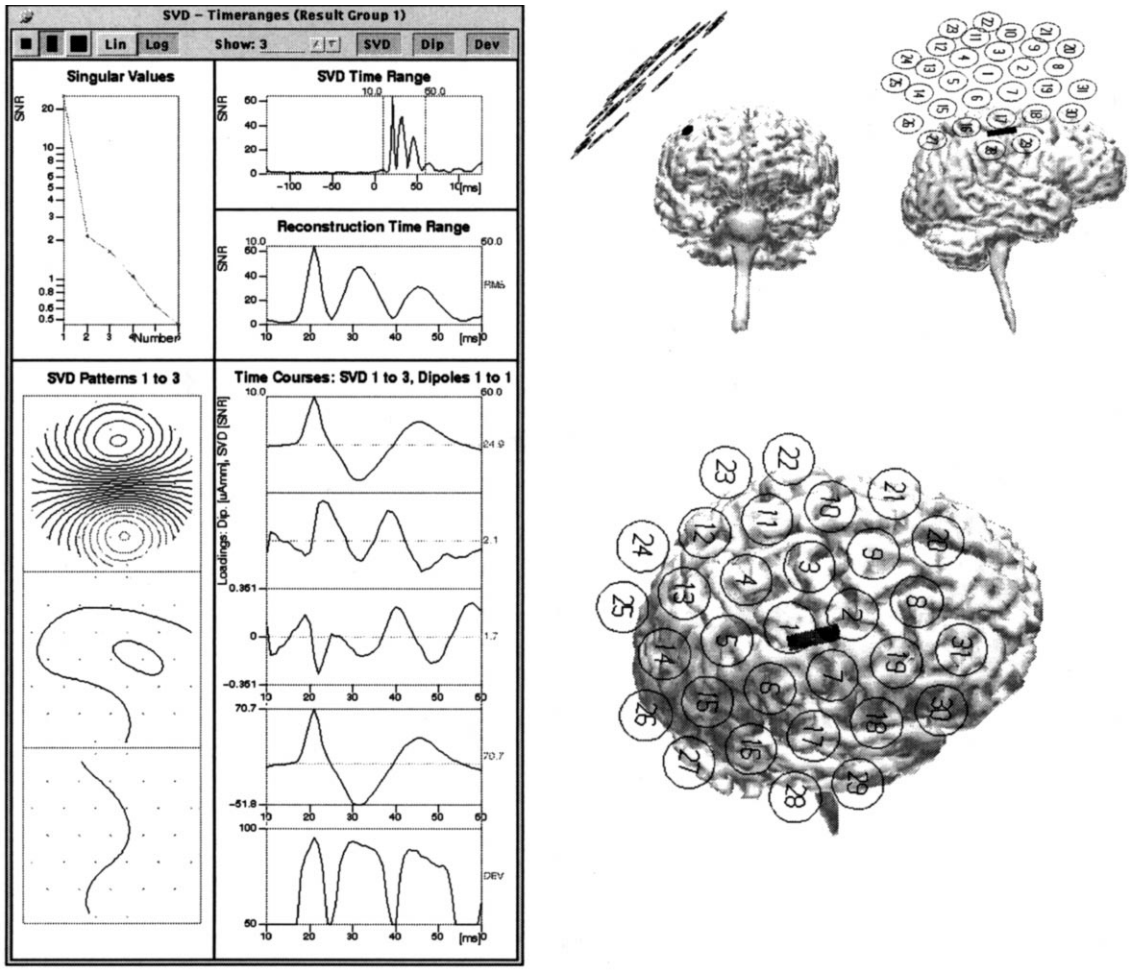

Fig. 11. Spatiotemporal analysis of the MEG data in the latency range of 10–60 ms. On the left side, the leading 3 SVD field patterns and loadings can be seen together with the loadings of one fitted fixed dipole and the explained deviation (lowest row). The right column displays the dipole position and orientation (shown as dark bar) overlaid to the cortical surface and the lower gradiometer pick-up coils in different projections.

This motivates the use of spatiotemporal models.

3.2.2. Spatiotemporal dipole reconstructions

Spatiotemporal dipole modeling was performed for the interesting latency range of 10–60 ms. SVD analyses of these time ranges revealed 3 significant field patterns in the EEG and one dominating pattern in the MEG case (Figs. 10 and 11). Since the number of field patterns corresponds to the minimum number of fixed source configurations that might be able to generate the data, at least 3 fixed dipoles are needed to explain the EEG data. In the EEG and in the combined case (Fig. 12) the dipoles were sequentially fitted in the latency ranges of 18–21 ms (tangential N20 dominating), 22–26 ms (radial P22 and decreasing N20), and the remaining small peak between 14 and 17 ms (deep source close to the brainstem (Buchner et al., 1995)). As can be seen in Figs. 10 and 12 and Table 2, these 3 dipoles were sufficient to explain the measured data reasonably well (best residual deviations about 10% (best explained variances about 99%). The deep source has its main loading at very early latencies (P16, lowest loading trace), next the tangentially-oriented source develops (N20, centered in the posterior wall of the central sulcus, upper loading trace), succeeded by the radial P22 (located in the postcentral gyrus (Buchner et al., 1996), middle loading trace).

The MEG data could be explained reasonably well with one single tangentially-oriented source in the posterior wall of the central sulcus, adding a second source did not improve the overall fit accuracy (lowest trace in Fig. 11). The optimization was carried out with a regularization parameter $\lambda \approx 1$, assuming that the SNRs are estimated correctly. A value of $\lambda = 1.5$ was adequate to suppress quasi-radial components in single latency MEG results (Figs. 8 and 9 and Table 1).

The results of the combined evaluation are displayed in Fig. 12. Qualitatively, the dipole positions look similar to the EEG localization results. The confidence intervals are smaller in the combined case (compare Fig. 9), since the larger number of sensors and the complementary nature of both modalities stabilize the results. Details about the dipole positions can be found in Table 2. The tangential dipole is localized equally well by all methods, whereas differences

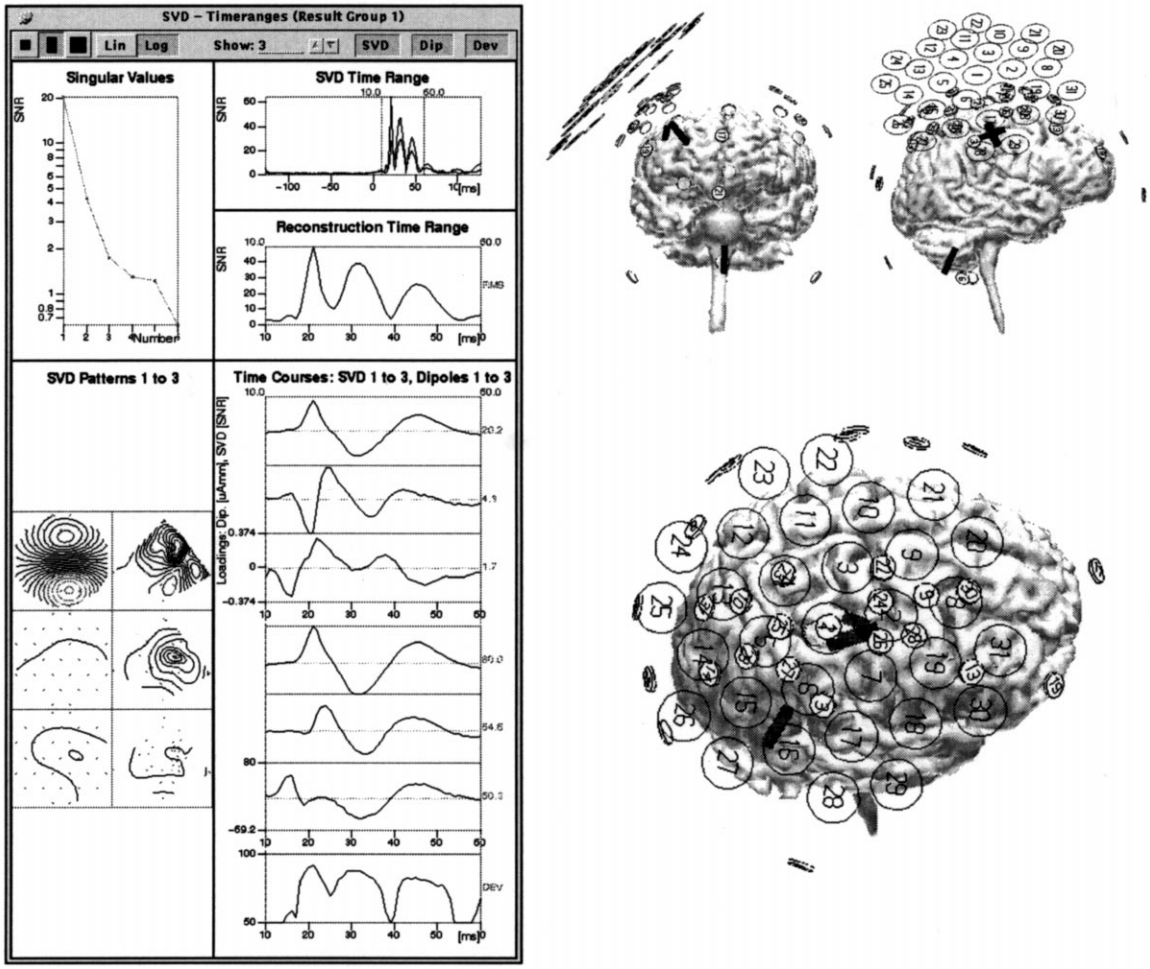

Fig. 12. Spatiotemporal analysis of the combined EEG + MEG data in the latency range of 10–60 ms. On the left side the leading 3 SVD field patterns and loadings can be seen together with the loadings of 3 sequentially fitted fixed dipoles and the explained deviation (lowest row). The right column displays the dipole positions and orientations (shown as dark bars) overlaid to the cortical surface and the sensors in different projections.

can be found for radial source position and especially for the deep (P16) dipole. The latter is most affected by regularization, due to the small SNR values (compared to the N20, P22 components) and the therefore rather large confidence volume of the dipole fit result at these very early latencies.

Finally, a cortically constrained MUSIC scan was performed over the same latency range. Three SVD patterns and thus the same number of fixed dipole components were taken into account. The result of the scan is displayed in Fig. 13 in a color-coded representation, overlaid to the cortical surface. A separation of the tangential and the radial source was not possible, nevertheless a more objective verification (that does not depend on the time-ranges used for the sequential fit procedure) of the results presented above could be achieved. A rather restricted area around the N20 and P22 dipole positions lights up in the MUSIC scan, whereas the deep P16 source is represented by a larger basal cortical patch centered around the brain-stem.

4. Conclusions

A framework for combining bioelectric and biomagnetic data on the basis of a signal-to-noise ratio transformation of the data was presented. Common realistic volume conductor models were used and a new regularization approach for the source reconstruction algorithms was introduced, using the partial variances that can be explained by the principal dipole components. In order to test and verify the methods, extensive simulations were carried out. Normalized sensitivity and dipole resolution profiles for different EEG/MEG systems were extracted from these synthetic data. Improved spatial resolution of the combined data studies was revealed, which is due to the complementary nature of both modalities and the increased number of sensors, leading to improved data statistics.

The sensitivity and single dipole resolution characteristics of 19 different EEG/MEG set-ups (Fig. 2) were studied by simulating dipolar field-patterns. For all configurations and test dipole positions altogether 460 000 data-sets were

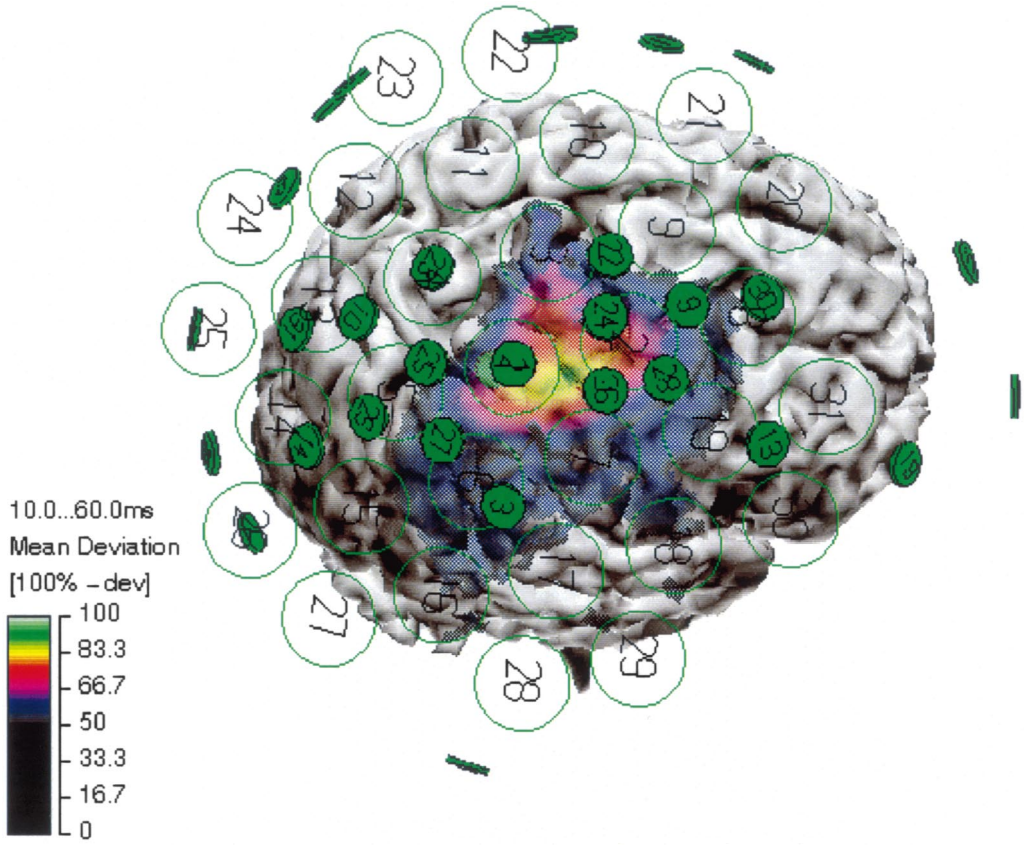

Fig. 13. Spatiotemporal MUSIC reconstruction of the combined EEG + MEG data in the latency range of 10–60 ms. For the cortically constrained MUSIC scan the leading 3 (combined) field patterns have been used. The result is shown as color-coded overlay onto the cortical surface together with the electrodes and the lower gradiometer pick-up coils.

derived by adding white noise of 5 different levels to the forward calculated fields. For each field-pattern of these synthetic data a dipole fit was performed, followed by averaging of the corresponding results in order to get statistically relevant conclusions.

Normalized mean SNR curves representing the system sensitivities were calculated by averaging (5*) 200 datasets per point (Figs. 4 and 5). The mean dipole mislocalizations were found to be inversely proportional to the corresponding mean SNRs for all sensor montages, so a normalized representation could be extracted (Figs. 6 and 7). This allows estimation of the confidence ranges of single dipole solutions, given the SNR of the data, the sensor set-up, and the depth of the fitted dipole. The shape of the confidence region can be studied by high spatial resolution deviation scans around the dipole location, that has been determined by the preceding fit (Fig. 9).

The expected behavior of combined EEG and MEG data was verified quantitatively by these simulations. Radial sources can by detected by EEG only. The sensitivity differences between radial and tangential dipoles are not as dramatic as in the magnetic case, but differ only by a factor of approximately 2 for deeper sources (Fig. 4). The depth dependency of the sensor gain is much weaker in the EEG cases, thus enabling still reasonable fit results for non-superficial, deeper dipoles. The MEG systems exhibit an improved resolution for superficial, tangential sources (Fig. 6).

It can be seen from Fig. 5 that for radial source orientations the SNRs drop faster than for tangential dipoles and thus the radial sources mislocalizations increase slightly faster with depth for all EEG montages. The larger the coverage, the better the localization accuracy for deeper sources. By comparing the 61 and 32 electrode montages, which have the same coverage, but different electrode densities, we found that for tangential dipoles the coverage is the most important factor (that determines the spatial resolution), whereas the set-up with the lower number of sensors is not well suited for localizing superficial radial sources, due to a spatial under-sampling of the electric field-patterns. MEG systems have superior resolution power for superficial tangential sources, but the SNRs drop sharply and the localization errors increase rapidly for deeper dipole positions.

The combination of both modalities gives overall improved results at all eccentricities (Figs. 5 and 7), due to the increased number of sensors and the complementary field distributions. For sources close to the center of the volume conductor the electric data dominate, at medium positions both modalities contribute, and for superficial positions an increasing influence of the magnetic data can

be found.

In order to verify the simulations with real measured data, we have analyzed simultaneously acquired SEP/SEF data at very early latencies with single dipole reconstructions, cortically constrained deviation scans, spatiotemporal, multiple dipole models, and compared single and combined modality results. All approaches revealed dipolar sources in the right central sulcus area, which should of course be expected from left hand medianus nerve stimulation. The combined EEG + MEG evaluations exhibit the best spatial resolution with a smooth transition between both tangential and radial dipole orientations, whereas the magnetic data alone contain information of the tangential source only. The electric data alone in this case suffer from smaller SNRs and less spatial resolution due to volume conductor effects and large inter-electrode distances.

Merged EEG/MEG evaluations thus indeed promise increased localization accuracy and a better understanding of the underlying neuronal processes, since also a better differentiation between (quasi-) tangential and (quasi-) radial source components is possible.

References

Ben-Isreal, A. and Greville, T.N.E. Some topics in generalized inverses of matrices. In: M.Z. Nashed (Ed.), Generalized Inverses and Applications, Proc. of an Advanced Seminar Sponsored by the Mathematics Research Center. Academic Press, New York, 1976, pp. 125–147.

Buchner, H., Fuchs, M., Wischmann, H.-A., Dössel, O., Ludwig, I., Knepper, A. and Berg, P. Source analysis of median nerve and finger stimulated somato-sensory evoked potentials: multichannel simultaneous recording of electric and magnetic fields combined with 3D-MR tomography. Brain Topogr., 1994, 6: 299–310.

Buchner, H., Waberski, T.D., Fuchs, M., Wischmann, H.-A., Beckmann, R. and Rienäcker, A. Origin of P16 median nerve SEP component identified by dipole source analysis – subthalamic or within the thalamo-cortical radiation?. Exp. Brain. Res., 1995, 104 (3): 511–518.

Buchner, H., Waberski, T.D., Fuchs, M., Drenckhahn, R., Wagner, M. and Wischmann, H.-A. Postcentral origin of P22: evidence from source reconstruction in a realistically shaped head model and from a patient with a postcentral lesion. Electroenceph. clin. Neurophysiol., 1996, 100: 332–342.

Cohen, D. and Cuffin, B.N. Comparison of the magnetoencephalogram and electroencephalogram. Electroenceph. clin. Neurophysiol., 1979, 47: 132–146.

Cohen, D. and Cuffin, B.N. Demonstration of useful differences between magnetoencephalogram and electroencephalogram. Electroenceph. clin. Neurophysiol., 1983, 56: 38–51.

Cohen, D. and Cuffin, B.N. A method for combining MEG and EEG to determine the sources. Phys. Med. Biol., 1987, 32 (1): 85–89.

Cohen, D., Cuffin, B.N., Yunokuchi, K., Maniewski, R., Purcell, C., Cosgrove, G.R., Ives, J., Kennedy, J.G. and Schomer, D.L. MEG versus EEG localization test using implanted sources in the human brain. Ann. Neurol., 1990, 28 (6): 811–817.

Cohen, D. and Cuffin, B.N. EEG versus MEG localization accuracy: theory and experiment. Brain Topogr., 1991, 4 (2): 95–103.

Crowley, C.W., Greenblatt, R.E. and Khalil, I. Minimum norm estimation of current distributions. In: S.J. Williamson, M. Hoke, G. Stroink and M. Kotani (Eds.), Advances in Biomagnetism. Plenum Press, New York, 1989, pp. 603–606.

Cuffin, B.N. Effects of head shape on EEGs and MEGs. IEEE Trans. Biomed. Eng., 1990, 37 (1): 44–52.

Ferguson, A.S., Zhang, X. and Stroink, G. A complete linear discretization for calculating the magnetic field using the boundary element method. IEEE Trans. Biomed. Eng., 1994, 41 (5): 455–460.

Fletcher, D.J., Amir, A., Jewett, D. L and Fein, G. Improved method for computation of potentials in a realistic head shape model. IEEE Trans. Biomed. Eng., 1995, 42 (11): 1094–1104.

Fuchs, M., Wagner, M., Wischmann, H.-A., Ottenberg, K. and Dössel, O. Possibilities of functional brain imaging using a combination of MEG and MRT. In: C. Pantev (Ed.), Oscillatory Event-Related Brain Dynamics. Plenum Press, New York, 1994, pp. 435–457.

Fuchs, M., Wischmann, H.-A., Wagner, M. and Krüger, J. Coordinate system matching for neuromagnetic and morphological reconstruction overlay. IEEE Biomed. Eng., 1995, 42 (4): 416–420.

Fuchs, M., Wischmann, H.-A., Wagner, M., Drenckhahn, R. and Köhler, Th. Source reconstructions by spatial deviation scans. In: C. Aine, Y. Okada, G. Stroink, S. Swithenby and C. Wood (Eds.), Advances in Biomagnetism Research: Biomag96, Springer-Verlag, New York, 1998a, in press.

Fuchs, M., Drenckhahn, R., Wischmann, H.-A. and Wagner, M. An improved boundary element method for realistic volume conductor modeling. IEEE Trans. Biomed. Eng., 1998b, 45: in press.

Geddes, L.A. and Baker, L.E. The specific resistance of biological material, a compendium of data for the biomedical engineer and physiologist. Med. Biol. Eng., 1963, 5: 271–293.

Geselowitz, D.B. On bioelectric potentials in an inhomogeneous volume conductor. Biophys. J., 1967, 7: 1–17.

Geselowitz, D.B. On the magnetic field generated outside an inhomogeneous volume conductor by internal current sources. IEEE Trans. Magn., 1970, MAG-6: 346–347.

Greenblatt, R.E. Combined EEG/MEG source estimation methods. In: C. Baumgartner, L. Deecke, G. Stroink and S.J. Williamson (Eds.), Biomagnetism: Fundamental Research and Clinical Applications. Elsevier, Vienna, Austria, 1993, 1995, pp. 402–405.

Gorodnitzky, I, George, J.S, Schlitt, H.A. and Lewis, P.S. A weighted iterative algorithm for neuromagnetic imaging. Proc. IEEE Satellite Symposium on Neuroscience and Technology, Lyon, 1992, pp. 60–64.

Hämäläinen, M.S. and Sarvas, J. Realistic conductivity geometry model of the human head for interpretation of neuromagnetic data. IEEE Trans. Biomed. Eng., 1989, 36 (2): 165–171.

Hansen, P.C. Analysis of discrete ill-posed problems by means of the L-curve. SIAM Rev., 1992, 34 (4): 561–580.

Köhler, T., Wagner, M., Fuchs, M., Wischmann, H.A., Drenckhahn, R. and Theißen, A. Depth normalization in MEG/EEG current density imaging. In: H.B.K., Boom, C.J. Robinson and W.L.C. Rutten (Eds.),. Proc. IEEE Eng. Med. and Biol., Nijmegen, The Netherlands, 1996, paper 144.

Lawson, C.L. and Hanson, R.J. Solving Least Squares Problems. Prentice-Hall, Englewood Cliffs, NJ, 1974.

Lopes da Silva, F.H., Wieringa, H.J. and Peters, M.J. Source localization of EEG and MEG: empirical comparison using visually evoked responses and theoretical considerations. Brain Topogr., 1991, 4 (2): 133–142.

Mauguiere, F. A consensus statement on relative merits of EEG and MEG. Electroenceph. clin. Neurophysiol., 1992, 82 (5): 317–319.

Menninghaus, E. and Lütkenhöner, B. How silent are deep and radial sources in neuromagnetic measurements? In: C. Baumgartner, L. Deecke, G. Stroink and S.J Williamson (Eds.), Biomagnetism: Fundamental Research and Clinical Applications. Elsevier, Vienna, Austria, 1993, 1995, pp. 352–356.

Mosher, J.C., Lewis, P.S. and Leahy, R.M. Multiple dipole modeling and localization from spatio-temporal MEG data. IEEE Trans. Biomed. Eng., 1992, 39 (6): 541–557.

de Munck, J.C. The potential distribution in a layered anisotropic spheroidal volume conductor. J. Appl. Phys., 1988, 64 (2): 464–470.

de Munck, J.C. A linear discretization of the volume conductor boundary

integral equation using analytically integrated elements. IEEE Trans. Biomed. Eng., 1992, 39 (9): 986–990.

Nelder, J.A. and Mead, R. A simplex method for function minimization. Comput. J., 1965, 7: 308–313.

Oostendorp, T.F. and van Oosterom, A. Source parameter estimation in inhomogeneous volume conductors of arbitrary shape. IEEE Trans. Biomed. Eng., 1989, 36 (3): 382–391.

van Oosterom, A. and Strackee, J. The solid angle of a plane triangle. IEEE Trans. Biomed. Eng., 1983, 30 (2): 125–126.

Pflieger, M.E., Simpson, G.V., Ahlfors, S.P. and Ilmoniemi, R.J. Superadditive information from simultaneous MEG/EEG data. In: C.Aine, Y. Okada, G. Stroink, S. Swithenby and C. Wood (Eds.), Advances in Biomagnetism Research: Biomag96, Springer-Verlag, New York, 1998, in press.

Press, W.H., Teukolsky, S.A., Vetterling, W.T. and Flannery, B.P. Numerical Recipies in C: The Art of Scientific Computing, 2nd edn. Cambridge University Press, New York, 1992.

Sarvas, J. Basic mathematical and electromagnetic concepts of the biomagnetic inverse problem. Phs. Med. Biol., 1987, 32 (1): 11–22.

Scherg, M. and von Cramon, D. Two bilateral sources of the late AEP as identified by a spatio-temporal dipole model. Electroenceph. clin. Neurophysiol., 1985, 65: 32–44.

Schlitt, H.A., Heller, L., Aaron, R., Best, E. and Ranken, D.M. Evaluation of boundary element methods for the EEG forward problem: effect of linear interpolation. IEEE Trans. Biomed. Eng., 1995, 42 (1): 52–58.

Wagner, M., Fuchs, M., Wischmann, H.-A., Ottenberg, K. and Dössel, O. Cortex segmentation from 3D MR images for MEG reconstructions. In: C. Baumgartner, L. Deecke, G. Stroink and S.J. Williamson (Eds.), Biomagnetism: Fundamental Research and Clinical Applications. Elsevier, Vienna, Austria, 1993, 1995, pp. 433–438.